minerals

MDPI

Article

In Vivo X-ray Computed Tomography Investigations of Crack Damage Evolution of Cemented Waste Rock Backfills (CWRB) under Uniaxial Deformation

Yu Wang [1,*], Changhong Li [1,*], Zhiqiang Hou [1], Xuefeng Yi [1] and Xiaoming Wei [2]

[1] Beijing Key Laboratory of Urban Underground Space Engineering, Department of Civil Engineering, School of Civil and Resource Engineering, University of Science and Technology Beijing, Beijing 100083, China; houzq_ustb@126.com (Z.H.); yxfeng_ustb@sina.com (X.Y.)

[2] Beijing General Research Institute of Mining and Metallurgy Technology Group, Beijing 102628, China; wxming_ustb@163.com

* Correspondence: wyzhou@ustb.edu.cn (Y.W.); lch_ustb@126.com (C.L.); Tel.: +86-010-623-2939 (Y.W.); +86-010-623-374 (C.L.)

Received: 15 October 2018; Accepted: 15 November 2018; Published: 21 November 2018

Abstract: Cemented waste rock backfill (CWRB), which is a mixture of tailings, waste rock, cement, and water, is subjected to combination actions in underground mining operations and has been widely used in deep resource mining. While the strength requirement and macroscopic deformation behaviors of CWRB have been well studied, the mesoscopic damage evolution mechanisms are still not well understood. In this work, a CWRB sample with a waste rock proportion of 30% was studied with a uniaxial compression test under tomographic monitoring, using a 450 kV industrial X-ray computed tomography (CT). Clear CT images, CT value analysis, crack identification, and extraction reveal that CWRB damage evolution is extremely inhomogeneous and affected by the waste rock size, shape, and distribution. Furthermore, the crack initiation, propagation, and coalescence behaviors are limited to the existing waste rocks. When deformation grows to a certain extent, the cracks demonstrate an interlocking phenomenon and their propagation paths are affected by the waste rocks, which may improve the ability to resist compressive deformation. Volumetric dilatancy caused by the damage and cracking behavior has closed a link with the meso-structural changes, which are controlled by the interactions between the waste rocks and the cemented tailing paste.

Keywords: cemented waste rock backfill (CWRB); X-ray CT; crack damage evolution; meso-structure change

1. Introduction

Due to the exhaustion of shallow mineral resources, the exploitation of deep mining resources is in urgent need. The deep mining process involves the removal of waste material from rock mass and the recovery of economically useful minerals [1,2]. Mining activity results from formation of plenty of underground gobs. In addition, waste material (e.g., tailing, waste rocks) has serious influence on the environment. Therefore, a technology of backfilling is usually expected to fill the underground cavities by using the waste materials from the mining process [2–5]. Many backfilling technologies have been used in the mining industry, such as cemented paste backfill (CPB), hydraulic sand backfill, and waste solid backfill. The CPB mining technology refers to the method of backfilling the underground gobs by mixing waste materials and binding material together and pumping them underground [2]. It is usually characterized as a mixture of mill tailings and water. If waste rock blocks are added to the backfill material, this backfilling method is then considered to be cemented waste rock backfill (CWRB) technology. The underground dispose of backfill has many advantages in mining engineering,

such as its excellent underground pressure control, rock burst control, ground support, stope stability maintain, ground water resource protection, less surface discharge of tailings waste, and favorable mining economics [5,6].

It is well known that strength is one of the most important factors considered in the design of backfill operation, especially when backfill plays the role of the supporting pillar, which ensures the safety of subsequent mining. For the CPB material, many scholars have conducted laboratory investigates using artificial or field CPB samples to study strength properties. In addition, large-scale numerical simulations have also been conducted for the mining stope. To ensure the safety of mining development, the required strength of CPB has been the focus for scholars and engineers all over the world. Through the laboratory uniaxial compression test, Belem and Benzaazoua [7,8] found that the uniaxial compressive strength(UCS) of the backfill, which ranged between 0.2 and 0.4 MPa. Cui and Fall [9] proposed an elasto-plastic model to consider the role of binder hydration in the evolution of CPB mechanical behaviors; the reliability of the model was verified by laboratory tests. Cayouette [10] and Fahey et al. [11] have tested the UCS of samples obtained through in-situ coring of backfill, finding that the UCS value of in-situ backfill samples is larger than the laboratory results. Chen et al. [12] performed an experiment to study the strength of CPB in a similar stope model, which revealed the change rule at different positions in the model. Cao et al. [13] studied strength and micro-structural properties of CPB, revealing CPBs strength evolution characteristics. Taheri et al. [14] performed a mechanical experiment to investigate the influence of loading histories and testing conditions on CPB stress strain behaviors. Wu et al. [15] studied the influence of particle size distribution and confining pressure on the peak strength of CPB. Their results showed that the peak strength of CPB is positively linear with confining pressure, as well as an optimal gradation of particles leading to the maximum strength of CPB.

The UCS of CPB is influenced by many factors, such as the composition, confining pressure, curing condition, curing time, and binding material characteristics [3,4,16–22]. To improve the mechanical properties of CPB, many experiments have been conducted to improve the hydraulic performance of the binder. For example, fly ash and silica fume has been added to ordinary Portland cement [23–25]. Characteristics of binder material is the determinant factor affecting the mechanical properties of CPB. Xu et al. [24] investigated the strength and microstructure evolution of CPB with different binder types and contents. However, in practical engineering, economic benefits are closed and related to the type, dosage, and acquisition. An alternative backfill technology to improve the strength and stiff of CPB is to add waste rocks into CPB [26]. CWRB has many advantages over CPB; CWRB treats waste rocks during mining, but also makes full use of the mineral resources. The issue of ore loss and dilution can be reduced by using CWRB, as the mining can achieve high efficiency, high duty, and high utilization characteristics.

Many experimental investigations have been conducted to reveal the mechanical properties of CWRB. Hane and Belem [26] performed UCS testing to reveal the influence of waste block proportion on strength and deformation characteristics. They found that the strength of the sample could be improved by adding waste rocks to the mixture. Taheri and Tatsuoka [27] conducted multiple-step triaxial compression experiments in order to study the strength and deformation characteristics of cement-mixed gravelly soil. They found that stress–strain relations during reloading became proportionally softer and observed an increase in negative axial strain increments. Wu et al. [28] conducted UCS testing to study the mechanical characteristics of cemented waste rock backfills with continuous particle gradation and found that the strength of the sample increased with the decrease of the backfill porosity. In addition, they found that the UCS of cemented waste rock backfills waslarger than samples with no waste rock blocks. He et al. [29] performed uniaxial compression tests to obtain the strength of the backfills with seven different mixture ratios at different solidification durations. The strength of the backfills sample after 28 days curing was selected as a basic parameter to simulate the stability of stope. He et al. [30] also obtained the UCS of the CWRB with different curing duration and established corresponding damage theory models, as well as forming the energy

dissipation equations of cemented waste rock backfill and surrounding rock. Liu et al. [31] studied the strength characteristics of CWRB samples under a low temperature condition. The results showed that adding waste block can improve slurry density and found that lower temperatures hinder hydration. The strength of the backfill sample was strongly influenced by the curing temperature and curing duration.

The required strength of CWRB is an important parameter during mining design. Apart from the strength characteristics, the damage and deformation process of CWRB are critical to ensuring gob stability. In recent years, the failure characteristics of CWRB under different stress paths have been studied. In CWRB, the interactions between the cemented paste tailing and waste rock are known to be the main factors controlling its failed behavior [26]. The high elastic contrast between the cemented tailing paste and the waste rock indicates that damage would occur at the tailing paste-waste rock interfaces. In order to reveal the mechanical behavior of CWRB, most laboratory experiments on the sample strength and macroscopic stress–strain responses have been widely performed. Although mapping the internal strain field is impossible, the study scale of such experiments is based on the entire sample, because after the experiment, we can only observe the macroscopic failure morphology under the naked eye.

In recent years, different non-destructive techniques have successfully been used to investigate the in-situ damage cracking mechanism of CWRB. Such studies include the acoustic emission (AE) monitoring of the occurrence and location of cracking events, which reveal damage evolution and locate fracture positions. Du et al. [32] conducted uniaxial compression tests for cemented coal waste backfill samples, where the failure process of the samples was monitored using an AE positioning technique. Anay et al. [33] used the AE method to monitor the formation and coalescence of micro-cracks in cement paste samples. The AE data was further corrected by micro-CT scanning the sample after failure. Assi et al. [34] used AE technology to study the early hydration of a kind of Portland cement paste, exploring the relationship between the recording signals related to elastic stress waves and the potential mechanism related to cement hydration. Another effective and non-destructive technique is the X-ray computed tomography (CT), which can provide real-time information on the changes of some physical parameters in the samples during the experiment. This technique has been widely used in soil, rock-like, or rock material [35–38]. Although many effects have been done to explore the mechanical behaviors of CWRB, the application of X-ray CT that investigates mesoscopic damage evolution behavior is not common. After the literature review, it can be found that the studies regarding the meso-damage evolution process of CWRB are rarely reported. However, investigating the meso-structural changes during deformation and revealing the associated meso-damage characteristics of CWRB is significant to the stability prediction of pillars and ground pressure control during mining.

The main motivation of this work is to experimentally reveal the mesoscopic damage and cracking mechanism of the CWRB under uniaxial compression, using a special self-designed loading apparatus combined with the X-ray computed tomography technique. The uniaxial stress strain responses of CWRB were studied from a macroscopic perspective. In addition, meso-structural changes and the associated localized deformation of CWRB were analyzed from the mesoscopic view. This work emphatically investigates the mesoscopic damage evolution mechanism for CWRB under uniaxial compression at different loading stages.

2. Materials and Methods

2.1. Materials

2.1.1. Full Tailings and Binder

The full tailings were obtained from the iron plants located in the Lilou iron mine (Anhui province, China) (Figure 1). The relative density of the full tailings was measured according to the Chinese standard GB/T 208-94 [39].The particle size distribution of the tailings was measured with a CILAS1064 particle size analyzer (CILAS, Orleans, France) (Figure 2). We used a series of physical and chemical

properties to measure the full tailings (Table 1). The main mineral composition of tailings found using an X-Ray Powder Diffraction analysis (Rigaku, Tokyo, Japan) is shown in Figure 3.The heterogeneity of the tailing was characterized with the ratio D60 to D10, and was ultimately found to be 15.27. This result indicated that the gradation of the tailing was poor.

The binder used in the preparation of CWRB samples was a kind of Ordinary Portland Cement (OPC, 32.5), which was in accord with the Chinese National Standard GB 175-2007 [40]. The main components of the OPC were calcium aluminate, dicalcium silicate, calcium ferroaluminates, tricalcium silicate, and gypsum. The proportion of dicalcium silicate and tricalcium silicatewasroughly 25% and 51%, respectively. The material of the binder was added to the mixture to form a hydration reaction that resulted in gelation properties. In order to ensure good support capacity during mining, the cementation properties were required to make the CWRB condensed enough to enhance its mechanical behaviors. Another function of OPC was to improve lubrication of CWRB during preparation.

Figure 1. The filling plants of the Lilou iron mine.

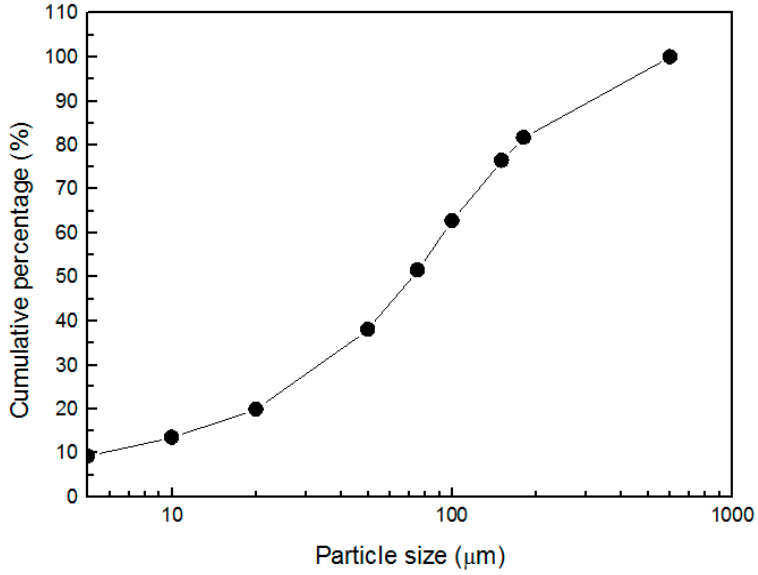

Figure 2. Particle size distributions of the Lilou full tailings.

Table 1. The basic physical and chemical parameters of the Lilou full tailings.

Index	Full Tailing (%)	Binder (%)
Physical properties		
Specific gravity (g/cm^3)	2.94	2.89
Natural density(g/cm^3)	1.351	N/A
Bulk density(g/cm^3)	1.732	N/A
Natural water content (%)	5.42	N/A
Porosity (%)	41.09	N/A
Natural repose angle (°)	41.5	N/A
Coefficient of uniformity, C_u	15.27	N/A
Coefficient of curvature, C_c	2.01	N/A
Chemical composition		
TFe	10.67	N/A
CaO	0.19	44.87
MgO	0.85	6.32
Al_2O_3	0.4	11.23
Fe_2O_3	8.8	1.241
SiO_2	76.85	27.88
SO_3	0.045	6.71
others	2.195	1.749

$C_c = D_{30}^2/(D_{10} \times D_{60})$; $C_u = D_{60}/D_{10}$.

2.1.2. Waste Rock

The waste rock was mostly composed of marble aggregates and acted as a coarse aggregate in the CWRB sample. It was sourced from the Lilou waste dump. In the test, the CWRB sample had a cylindrical shape with a size of Φ50 mm × H100 mm. According to the GB/T 50123-1999 [41], the required particle size of waste rock should be less than 10 mm. After a crushing treatment, the particle size of the waste rock was between 2 and10 mm. The proportion of the waste rock aggregates with a size between 6 and 8 mm was 65.7%, while the proportion of crushed waste rock between 2 and 6 mm was 35.3%. The natural density of the marble block was 2.66 g/cm^3. The UCS was 180.51 MPa.

2.1.3. XRD Studies

The mineral components of the Lilou iron full tailings were determined by the X-ray diffraction (XRD) method. The XRD machine was an Ultima-IV 3KW X and manufactured by the Japanese neo-confucian school. The results of the XRD testing is shown in Figure 3. Results reveals that the tailings were mainly composed of quartz, haematite, dolomite, and muscovite. By quantitative analysis, their proportions were 80.2%, 9.7%, 5.4%, and 2.6%, respectively. Because the elastic modulus of quartz crystal was relatively large, the corresponding compressibility was lower. Therefore, due to the high proportion of quartz in the tailings, the mechanical properties of the CWRB sample can be improved under compression, while the hematite, dolomite, and muscovite cause the material to be weathered easily.

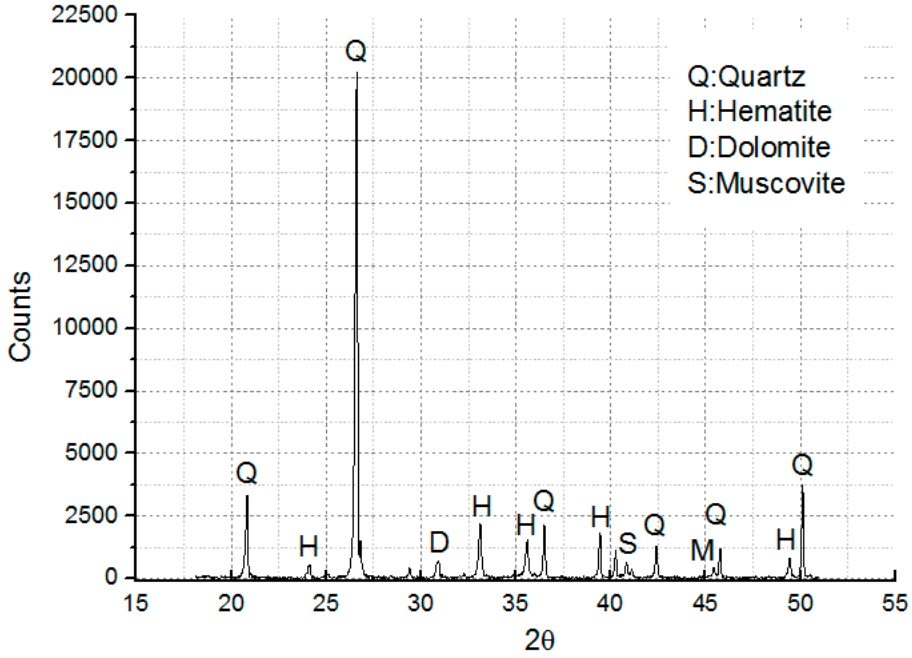

Figure 3. The X-ray diffraction (XRD) profile of the Lilou full tailings.

2.1.4. Sample Preparation and Mix Proportion

Tap water was used to mix the required amounts of tailings, binder, and waste rock. The ratio of the full tailings and binder was 1:8. According to the mining design, the waste rock proportion was designed to be 30% and the material pulp density was about 75%. In order to ensure the homogeneity, the mixtures were mixed in a double spiral mortar mixer for some minutes. Immediately after mixing, the mixtures were poured into a cylinder cast iron module with an inside diameter of 50 mm and height of 100 mm. The produced samples were then cured in a humidity chamber at 20 ± 1 °C with a relative humidity (RH) of 90% for 24 h (sealed). The samples were then demolded and placed in the same curing chamber under the same curing conditions for 28 days until conducing the mechanical testing. In this work, a total of 15 samples were prepared to conduct the laboratory studies.

2.1.5. SEM Analysis

For the cemented tailing paste, the scanning electron microscope (SEM) (Crossbeam 550, Zeiss, Berlin, Germany) method was used to reveal the mineral compositions and microstructure. Field emission scanning electron microscope (FE-SEM) (Crossbeam 550, Zeiss, Berlin, Germany) was used to conduct imaging. The resolution was 0.8 nm, acceleration voltage was between 0.02 and 30 kV, and the maximum magnification was 2 million times. Figure 4 shows the hydration and microstructure of the tailing paste after curing for 28 days. From the SEM results, it can be seen that three gray colors co-exist on the images and that the cemented tailing paste has strong heterogeneity. After obtaining the Electron Energy Disperse Spectroscopy (EDS) spectra for the three points on Figure 4a, we made the following conclusions: For point "1", Fe and O elements were detected, as this region represented the Fe element in the full tailings; for point "2", a percentage of the Si and O elements was larger than other elements, which indicated the uncemented tailing paste; for point "3", the proportion of the Ca, S, Al, and O elements was relatively large, indicating that the cemented regions experienced hydration reaction. From the SEM results and EDS spectra analysis, we found that the consolidation process of the full tailing paste included a series of process, such as hydration reaction, dissolution, accumulation, and hardening. When the tailing, binder, and water were mixed together, the $3CaO{\cdot}SiO_2$ and $2CaO{\cdot}SiO_2$ had a dissolution and hydration reaction, a process that generated lots of gel. This

sped up the cement reaction of the fine particle in the full tailing material, in which the strength of the cemented paste backfill will be improved accordingly.

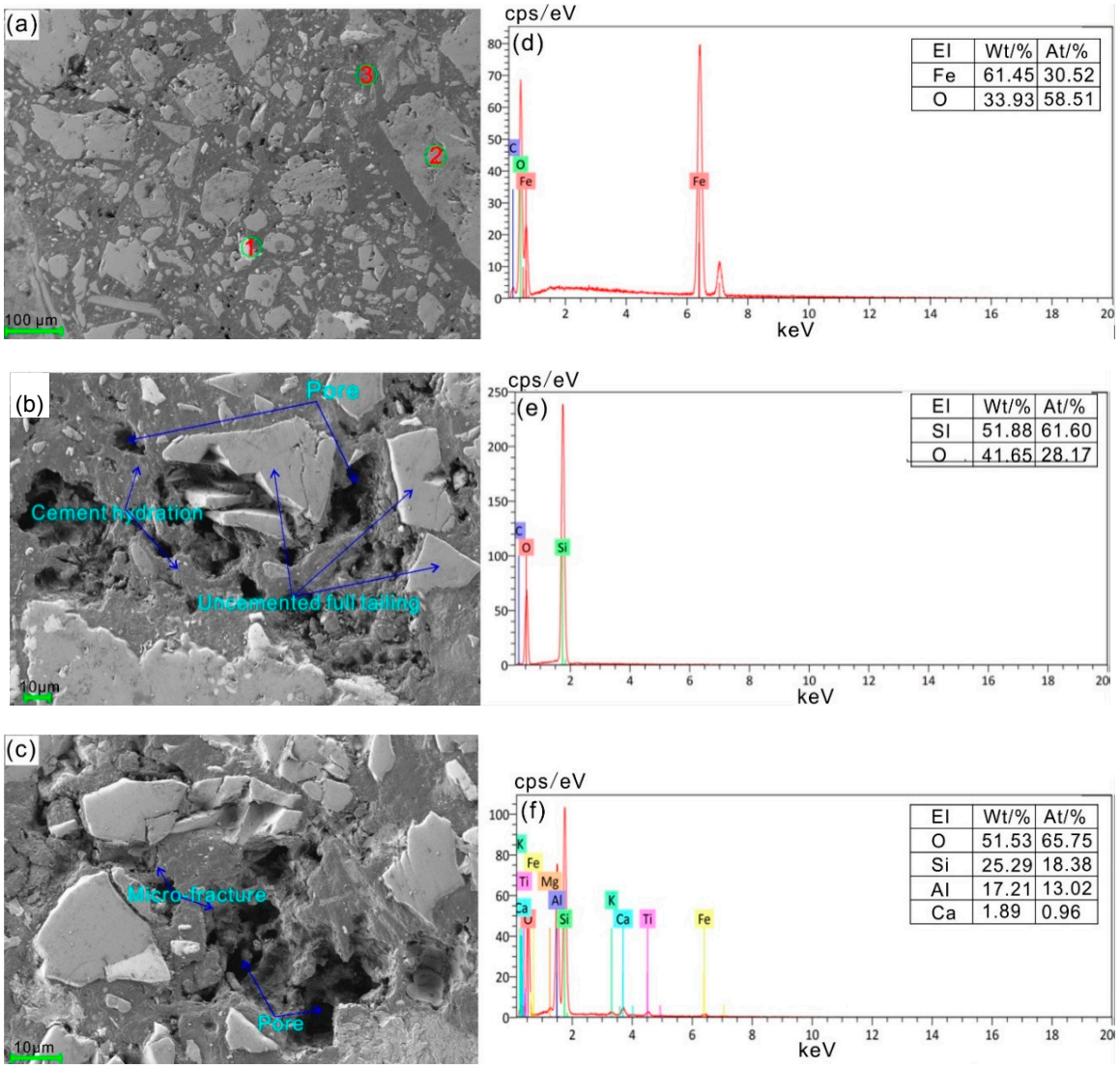

Figure 4. Scanning electron microscope (SEM) results for the cemented tailing paste (**a**–**c**): the magnification is 129, 627, and 1000 times, respectively; (**d**–**f**): for the three points on Figure 4a).

2.2. Experimental Apparatus

2.2.1. X-ray CT Device

A high energy 450 kV industrial X-ray CT machine (Made in China, by the Institute of High Energy Physics, Chinese Academy of Science) was used to obtain the CT images of the internal meso-structures in the CWRB sample subjected to uniaxial compression, as shown in Figure 5a. The working principle of the industrial X-ray CT is the same as the medical CT device. The principle of imaging is to record the X-ray radiographic images of a sample at several different angles. From these different projections, a virtual slice can be reconstructed using appropriate algorithms, either algebraic or via the in reverse projection principle. These algorithms add a few sequential slices together and then allow for reconstruction of a 3D object [35–37]. The system is composed of a focus X-ray source, an imaging intensifier detector coupled to CCD camera, a sample manipulator, and an image process unit. In this experiment, as the sample size was relatively large (Φ50 mm × H100 mm),a power setting of 420 kV and 2.0 mA was used for a 360° fan beam scan with 54,000 project views. The CWRB sample was

installed in the loading device mounted on a rotation table having high accuracy, then the detector was adjusted to fit the image within the field-of-view. Before conducting CT scans, the scanning parameters and conditions were calibrated and set to obtain high-resolution images and reduce the noise and artifacts during the image acquisition process.

Through rotating the object on a computer controlled rotation table, the X-ray attenuation equidistant records for different angles of 360°.The data is then reconstructed to create cross-sectional images of an object in the scanned plane. Each CT image is called a slice, because it can scan an object on the plane which seems to be cut off. Each slice or cross-sectional image consists of 1024×1024 pixels with a pixel size of 70 μm. Stacking up these slices together can create the 3D volume image of the scanned sample. The specification of the X-ray CT system is listed in Table 2.

Table 2. The detailed performance index of the 450 kV industrial X-ray computed tomography (CT) system.

Performance Parameter of the CT Device	Parameter	Unit
Effective scanning height	Φ1000	mm
Effective scanning diameter	Φ 800	mm
Maximum scanned weight	200	kg
Penetrate thickness for Fe	50	mm
Spatial resolution	0.07 × 0.07 × 0.07	mm^3
Perspective of relative sensitivity	1	%
Density resolution	0.1	%
Minimum scanning thickness	0.03	mm
Fastest scanning time	1	min
Image reconstruction time	30	s
Resolution capacity for crack	0.05×15	mm^2
Stomata resolution	Φ 0.3	mm
Resolution for inclusion	0.1	mm
Localization accuracy of the workbench	±0.02	mm
Accuracy of the turntable	±5°	s^{-1}

2.2.2. Loading Device

In order to keep track of the in-situ mechanical behaviors of the CWRB sample under the condition of the classical uniaxial test, a test apparatus is specially designed to meet the requirement of the CT machine. The loading apparatus consists of a reaction frame, a displacement measurement subsystem, and a load measuring subsystem. The reaction framework of the test apparatus should be transparent to X-rays and as a result is made of low-attenuated materials used for the reaction column, such as Poly Methyl Methacrylatemethacrylic Acid (PMMA) with a density of 1.16 g/cm^3. The PMMA material has good performance strength and stiff characteristics and has a kind of brittle and stiffness material. When subjected to tensile stress, the deformation is relatively small; its elongation at break is between 2% and 3%. For the PMMA material, the tensile strength, bending strength, compressive strength, and tensile modulus of PMMA range between 70 MPa, 130 MPa, 170 MPa, and 3100 MPa, respectively. The force measuring subsystem is battery-driven so as to avoid winding during the rotating of the CT rotation table. Figure 5b shows the loading apparatus used in the uniaxial compressive test.

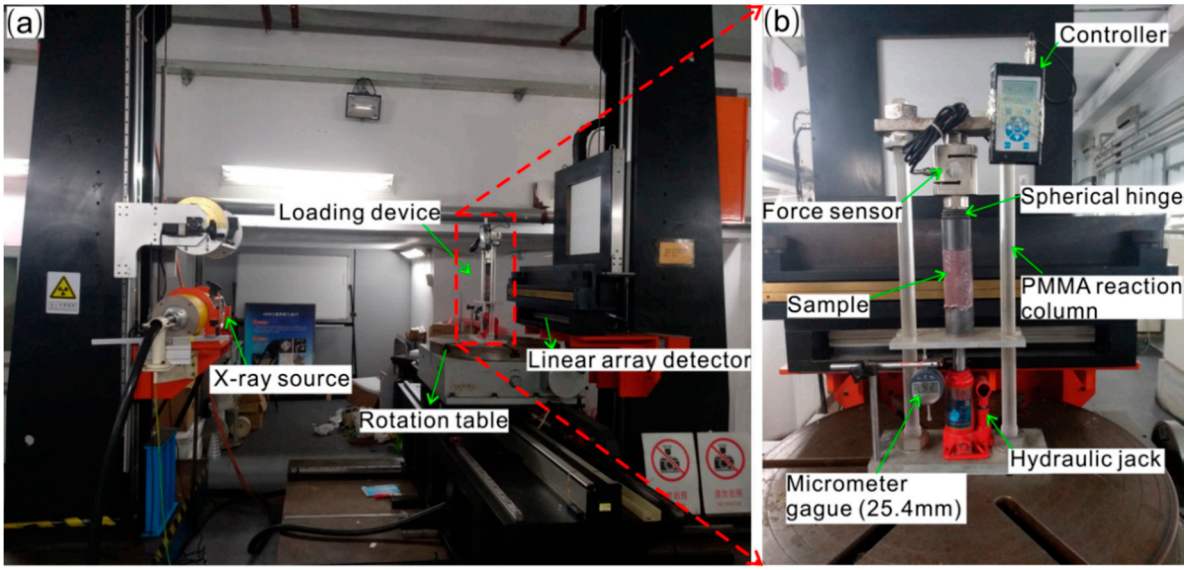

Figure 5. The testing system used for the cemented waste rock backfill (CWRB) sample. (**a**) Photo of 450 kV X-ray CT machine, which is mainly composed of X-ray source, rotation table, CCD, and detector; (**b**) Photo of the loading device, which is transparent to X-rays and composed of the force sensor, sample, micrometer, spherical hinge, PMMA reaction column, and hydraulic jack.

2.3. Testing Scheme

During the uniaxial deformation testing, the loading apparatus was first placed on the rotation table of the X-ray industrial CT machine. Then, the CWRB sample was installed on the loading device. The axial loading was then applied at a constant speed of 0.1 kN/s until the peak strength; after the peak strength, the loading was controlled by a displacement mode at a rate of 0.3 mm/s. The determination of the CT scanning stages was referred to the macroscopic stress strain curves in advances, as shown in Figure 6. Figure 6a plots the relationship between the axial stress and axial strain for the CWRB samples numbered as 1 to 6. From the macroscopic testing results, the maximum axial strain was1.15%. Therefore, when performing real-time the X-ray scanning testing, five scanning stages were chosen for the sixth CWRB sample, the corresponding axial strain is set to be 0, 0.5, 0.7, and 1.5 times of peak strain. Thus, the axial strain at the scanning point was0, 0.723, 1.16, 1.451, and 2.17, respectively, as shown in Figure 7.

The CT X-ray data were obtained from three central cross sections on the CWRB samples: the initial position was at 35 mm, 50 mm, and 65 mm along the sample, from the bottom to the top of the sample, as shown in Figure 8. It took nearly one minute to scan a single cross-section of the sample and two minutes to reconstruct a CT image. A total of 54,000 project views and 5 accumulations required an 18 min loading stage in the stress strain curve. When an X-ray CT scanning was performed, we stopped loading in order to keep the CWRB sample in a stationary state. After the completion of one CT scanning of a loading stage, the samples were loaded again with the same loading rate. It is important to note that stress relaxation phenomenon occurred at each scanning point on the stress-strain curve, as the axial displacement is fixed during the scanning process.

The data were composed of the radiological densities of each pixel, which could be visualized as a grayscale image on the grid, where each pixel was expressed with Hounsfield value. The gray scale had a dynamic range, which was suitable for the crack variation in the CWRB sample. Changes of the radiological density indicated the variation of the internal crack, which could be calculated from the Hounsfield value. When cracks appeared in the CWRB sample, the color displayed as black at the positions of the cracks.

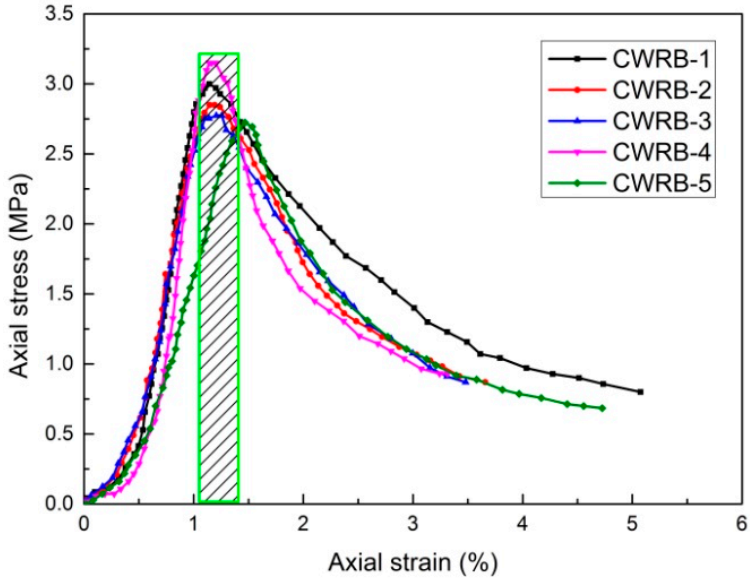

Figure 6. The macroscopic stress strain curves of CWRB sample 1–5, obtained by the GCTS RTR-2000 rock mechanics apparatus (GCTS, Tempe, AZ, USA).

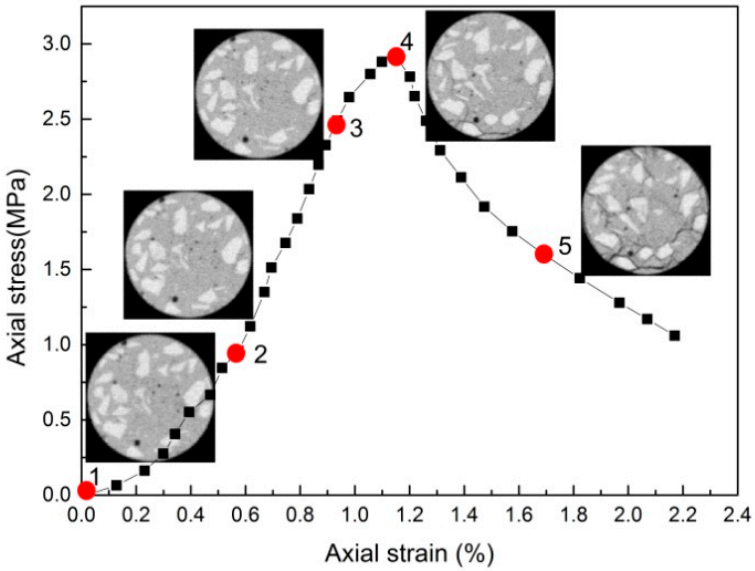

Figure 7. The axial stress strain curve for the CWRB-6 sample. The determination of the CT scanning stages refers to the macroscopic stress strain curve.

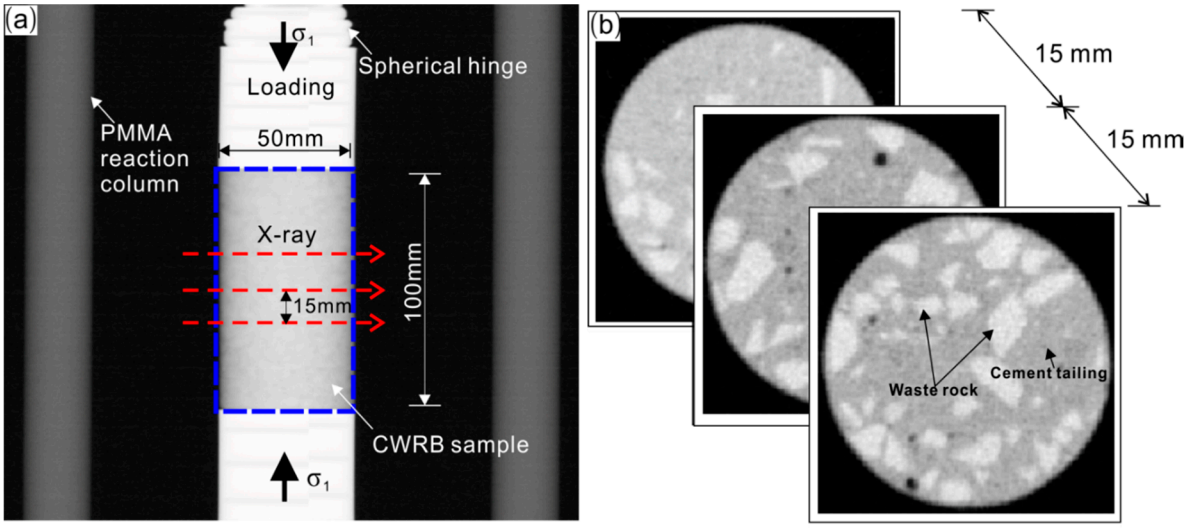

Figure 8. Scheme of X-ray CT scanning of the CWRB sample. (**a**) Perspective of the scanning position, the initial scanning position was 35 mm, 50 mm, and 65 mm; (**b**) Reconstructed CT images before loading.

3. Results and Discussion

3.1. General Observations

From the macroscopic stress strain curves (Figure 7), we did not know what happened during sample deformation. However, the meso-structural changes and the associated damage evolution was revealed using real-time X-ray CT scanning. The reconstructed CT images at different loading stages are shown in Figure 9. From the CT images, we observed that the waste rocks randomly distributed in the sample. According to the principle of CT imaging, the brighter the color, the higher density the material is. Due to the relatively high density of the waste rock, the gray level is brighter than the cemented tailing paste. Because the sample was not in a full compaction state, pores inside the sample displayed as black color and can also be seen clearly.

As the axial deformation grew, damage accumulated inside the sample. Due to the stiff contrast between the waste rock and the cemented tailing paste, when the deformation grew to a certain extent, the low-density region appeared. These regions were usually located at the interfaces of the waste rock and cemented tailing paste. From Figure 9, we can see that from the axial strain of 0.922%, the low-density region began to appear and the scale increased with an increasing sample deformation. When the axial strain reached 1.153% (peak strain), the low-density regions evolved into cracks, and could be clearly seen in the CT images. In the post-peak stage, when the axial strain was1.729%, the cracks distributed across the sample and their morphology was influenced by the geometry and distribution of the waste rocks. It can also be seen that the location of the low-density region was affected by waste rock distribution. Regions usually distribute around waste rock and then propagate into tailing paste.

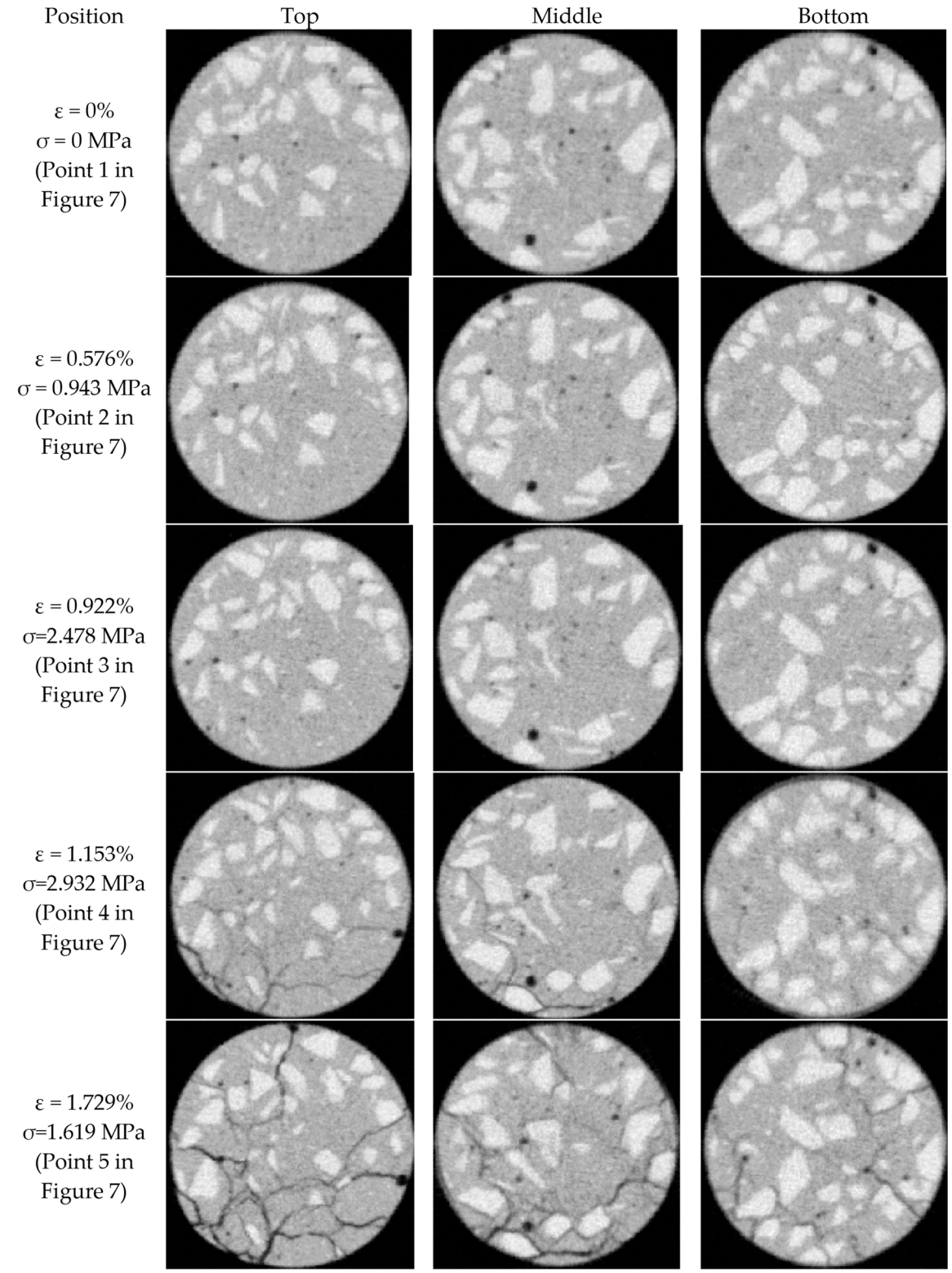

Figure 9. The reconstructed CT images of the CWRB sample at the top, middle, and bottom positions, under five loading stages in the stress strain curve.

3.2. Meso-Damage Propagation

The phenomenon of strain localization signified the onset of the failure in CWRB. In this section, we will analyze the damage evolution from the changes of micro-elements in the sample using an

index of the CT value that quantified the crack damage during the evolution process, revealing the mesoscopic damage mechanism.

The parameter of CT value had a close relationship with the rock density. Since a proportional relationship existed between the material density and the CT value, density distribution in the sample can be well characterized by the distribution of the CT value. To reveal the meso-damage evolution characteristics and study the localized deformation in the CWRB sample, three local regions of interest (ROIs) were chosen in the images, labeled as "1", "2", and "3"; the fourth ROI refers to the entire region of the sample section, as shown in Figure 10a–c. For the ROI1-3, the position in the image was determined to be located in the matrix zone so that we could ignore the effect of waste rock. Figure 10d,e depicts the relationship between the mean CT value, the deviation of the CT value, and the axial strain. From Figure 10d, the mean CT value first increased and then decreased as the axial strain grew. The results show that the CWRB sample experienced a compaction stage, a damage accumulation stage, and a crack propagation stage. When low-density regions appeared in the sample, the mean CT value began to decrease; when those regions evolved into cracks, the mean CT value decreased sharply. Figure 10e reflects the anisotropic damage characteristics, implying that the damage increased sharply and the localized deformation grew quickly to sample failure.

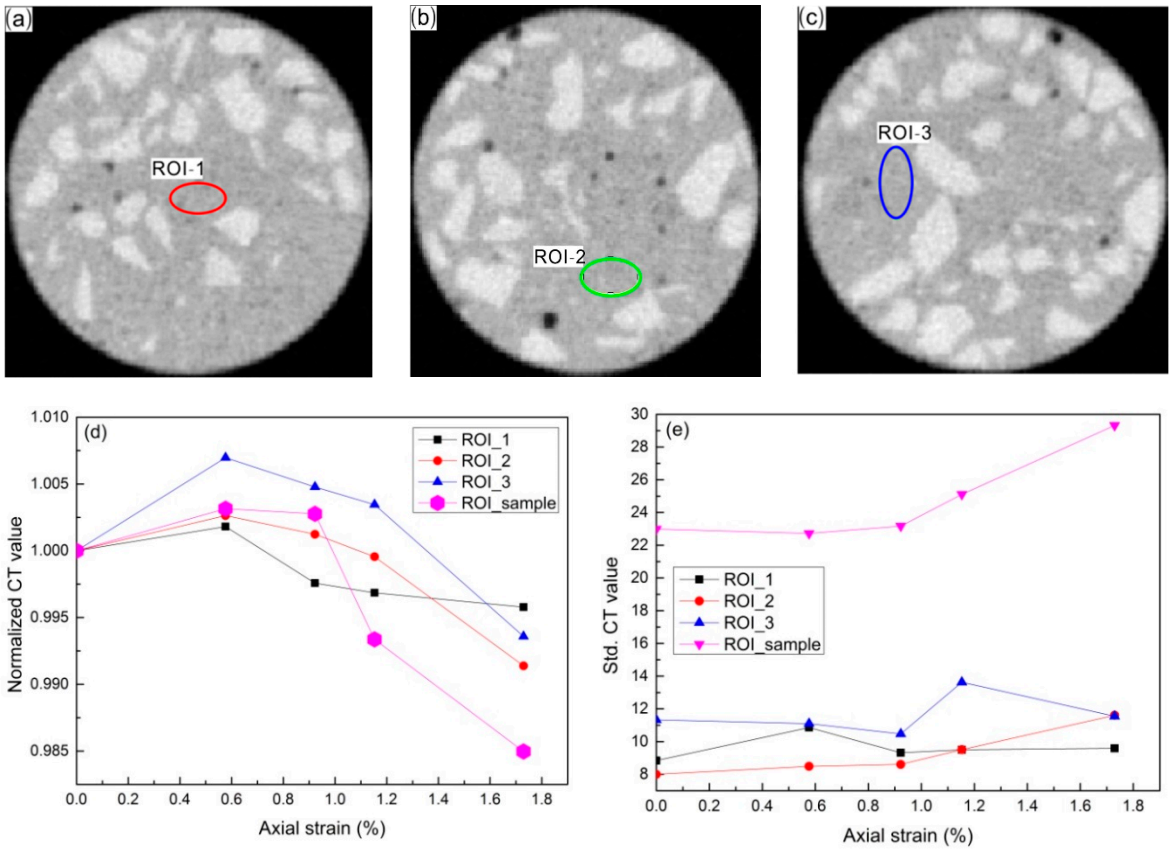

Figure 10. Meso-damage evolution of CWRB sample during deformation. (**a**–**c**) determination of the local region of interests, labeled as ROI-1, ROI-2, and ROI-3; (**d**,**e**): Relationships between the mean CT value, deviation of the CT value, and the axial strain.

3.3. Damage Evolution Model for CWRB

As stated above, the meso-damage in the micro-elements of a material can be described with the mean CT value. The index of the mean CT value is an important parameter commonly used to define the damage factor. According to the studies of Singh and Digby [42] and Lemaitre and Chaboche [43],

if the effects of the CT value on the damage variable are taken into account [44,45], the expression can be rewritten as:

$$D = \frac{1}{m^2}\frac{\Delta\rho}{\rho_0} \quad (1)$$

Where m is the space resolution of the used CT machine and $\Delta\rho$ is the variation in sample density during the damage evolution of the material, i.e., $\Delta\rho = \rho - \rho_0$.

We have known that there is a direct link between the CT value and density and therefore the damage factor can be rewritten as:

$$D = \frac{1}{m^2[H_0 - H_a]\rho_0}(H - H_0)(\rho_0 - \rho_a) \quad (2)$$

where H, H_a, H_0 are the CT value for the sample at any stress level, pore air, and initial state, respectively. For the CWRB sample, ρ_0 = 2.67 g/cm^3, ρ_a = 0 g/cm^3, H_a= −1000, m = 140 μm.

The damage evolution characteristics of the CWRB sample are listed in Table 3. When the axial strain changes from 0 to 0.576%, the mean CT value increased with the increase of normal stress. In this stage, the sample was under the compressive state and soft materials such as pores and microstructures were compacted. When the strain rose to 0.922%, damage began to occur in the CWRB sample. In addition, low-density regions evolved into cracks and cracks propagated and coalesced until the failure of the sample. The relation between the axial strain and the damage factor is plotted in Figure 11. The exponential function was used to fit their relationship, as shown in Equation (3), as well as the correlation coefficient of Equation (3), which was 0.903 and indicated a strong correlation between the damage factor (D) and the axial strain (ε), as expressed below:

$$D = 0.06142 \times e^{1.54464\varepsilon 1} \quad (3)$$

Referring to the equivalent strain principle [43,45], the constitutive model for the CWRB sample can be obtained as below:

$$\sigma_1 = E\,(1 - 0.06142 \times e^{1.54464\varepsilon 1})\varepsilon_1 \quad (4)$$

where E is the elastic modulus, ε_1 is the axial strain, and σ_1 is the axial stress.

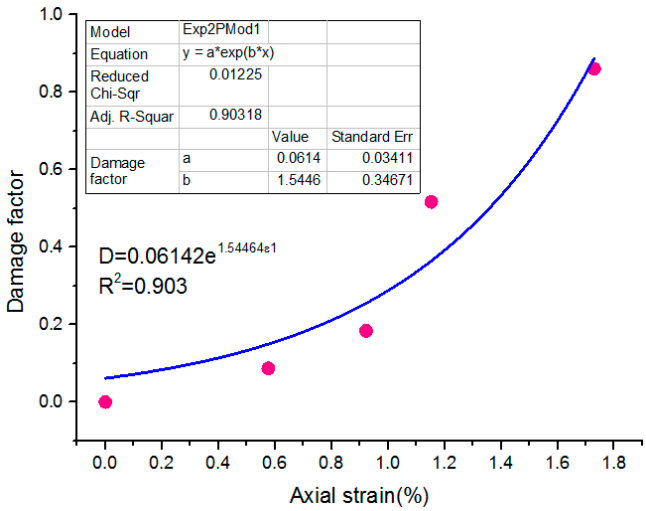

Figure 11. Plot of the damage factor against the axial strain. This was plotted to attain the damage evolution equation.

Table 3. Stress, strain, and mean of the CT value and the damage factor of the CWRB sample.

Loading Stage	ε_1 (%)	σ_1(MPa)	Mean CT Value	Damage Factor	Damage Behavior
1	0	0	714.52	0	No
2	0.576	0.943	716.77	0.087	Compression
3	0.922	2.478	716.78	0.184	Damage
4	1.153	2.932	709.78	0.517	Cracking
5	1.729	1.619	703.78	0.861	Propagation

Using Equation (4), the axial stress is obtained. We plot the experimental result and the fitting result in Figure 12, it can be seen that established result was closed with the experimental result. It should be noted that only the CT scan data were obtain (i.e., the top, middle, and bottom CT images) from three positions of the sample; more precise fitting results requires much more CT scan data.

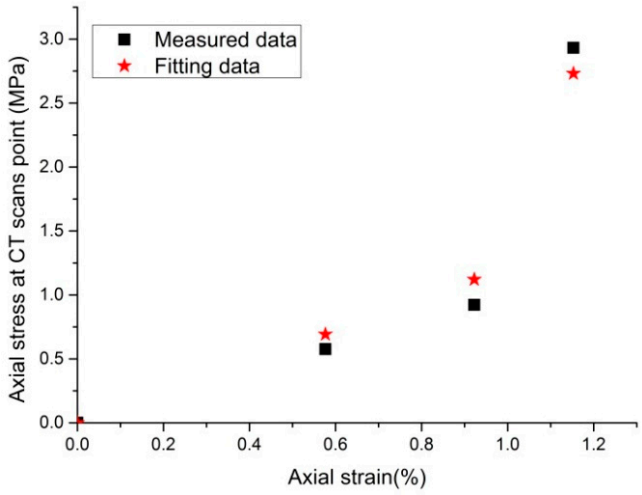

Figure 12. Comparison of the measured data and fitting data. The fitting results were obtained from the damage constitutive equation.

3.4. Meso-Structural Changes Analysis

The CT images were reconstructed based on the sample gray range. Using a series of digital imaging methods, the cracks could be identified and extracted from the images. During extraction of the cracks and waste rock, an algorithm named median filter was first used in order to detect the object boundary. Median filtering was especially useful for reducing the speckle noise, as well as the salt and pepper noise. The edge-preserve nature of this algorithm made it effective in detecting obscure edges, such as the irregular cracks in the CWRB sample. The filtering algorithm took the value of each output pixel as the median of the neighborhood value for the corresponding input pixel. We plotted the extracted waste rocks and cracks in the same figure (Figure 13). The scale and density of the cracks increased with each increasing sample deformation. Due to the waste rock, the propagation of the cracks was limited and an interlocking phenomenon occurs. This may have caused the improvement of strength compared to the cemented tailing paste. The propagation path of the crack negotiated most of the waste rocks, which implied that the macroscopic failure plane in CWRB was not planar but curved. The morphology of the cracks was strongly influenced by the waste block distribution and positions. Furthermore, we counted the total crack area and waste rock area, as shown in Figure 14. It can be seen that not only was the crack area increased as the deformation grew, but the waste rock area changed for the same scanning position. This result indicated that the movement and rotation of the waste rocks occurred during sample deformation. Localized deformation was largely attributed to the complicated motion of the waste rocks.

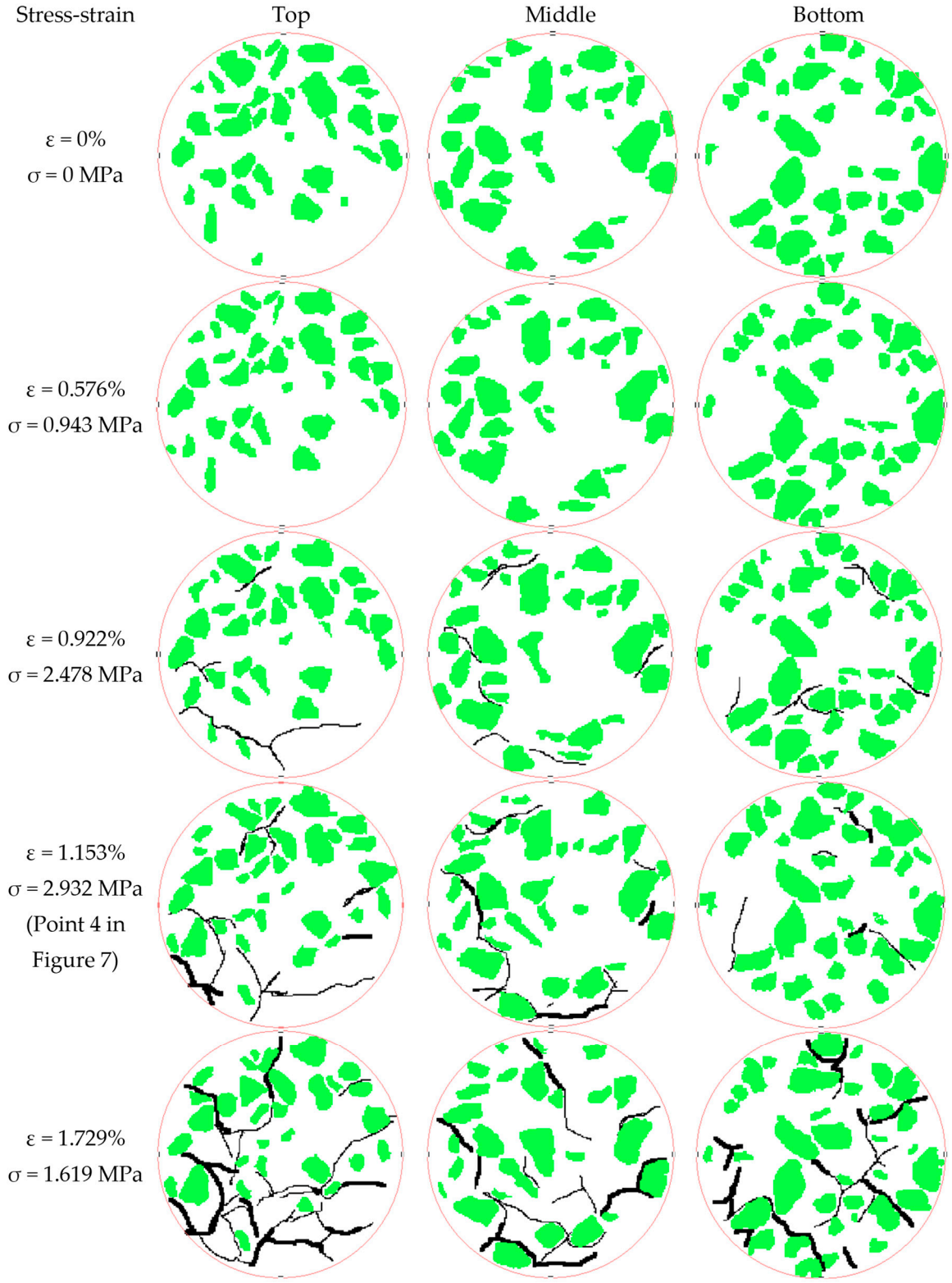

Figure 13. The extraction of waste rock and cracks on CT images under different deformation stages.

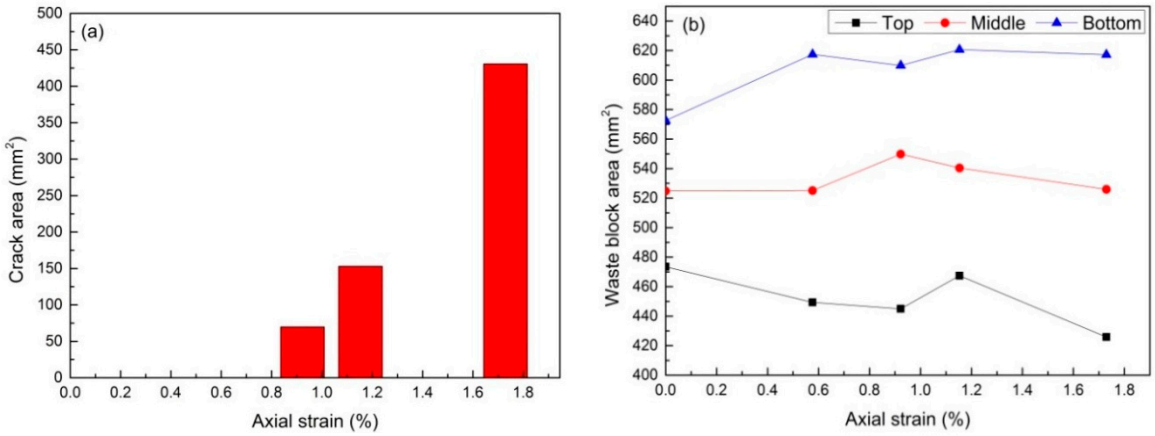

Figure 14. Structural changes in the CWRB sample during deformation. (**a**) Total crack area changes; (**b**) Changes of the waste rock content at the top, middle, and bottom scanning sections.

3.5. Dilatancy Characteristics

From the stress strain curve of the CWRB sample, plastic deformation increased with the increasing axial deformation. The stress strain curve in Figure 7 displays the macroscopic strain response of the entire sample scale. To study the stress dilatancy behavior of the CWRB sample, we emphatically analyzed the localized deformation from the mesoscopic view. The propagation of the low-density region in CT images indirectly reflected the volumetric change.

Table 4 shows the change of the section area for the three scanning sections at different loading stages. With the increase of deformation, especially from the third stage, the section area of CT images increased sharply under compression. Thus, the dilatation behavior became obvious. The volumetric expansion was owed to the occurrence of localized bands, which indicated the formation of a macroscopic fracture plane in the sample. From the reconstructed CT images in Figure 10, it can be also seen that the scale of the low-density region increased from the third loading stage.

Table 4. Stress-dilatancy characterization of the CWRB sample under uniaxial compression.

Loading Stage	Axial Strain (%)	Axial Stress (%)	Top Slice Δs(mm²)	Middle Slice Δs(mm²)	Bottom Slice Δs(mm²)
1	0	0	N/A	N/A	N/A
2	0.576	0.943	1.323	1.744	0.199
3	0.922	2.478	3.064	2.265	1.712
4	1.153	2.932	68.815	55.571	22.529
5	1.729	1.619	153.583	152.909	158.125

From the axial stress strain curve and the reconstructed CT images, the lateral and volumetric stress strain responses were obtained. The lateral strain and axial strain were defined as $\varepsilon_l = \Delta D/D_0$; $\varepsilon_a = \Delta L/L_0$. D_0, and L_0werethe initial sample height and diameter; ΔL and ΔD were the variations of the sample height and diameter during deformation; ΔD was obtained from the change of the section area of CT images. The volumetric strain was calculated as $\varepsilon_v = \varepsilon_a + 2\varepsilon_l$. Figure 15 plots the axial, lateral, and volumetric stress strain curves at the five scanning key points for the studied CWRB sample. It can be seen that volumetric strain changed from shear shrinkage to dilatancy. Accordingly, volume of the sample changed from compression to expansion at the third loading stage (corresponding to the third CT scans). After the inflection point, the dilatancy behavior became more and more severe to the failure of the sample.

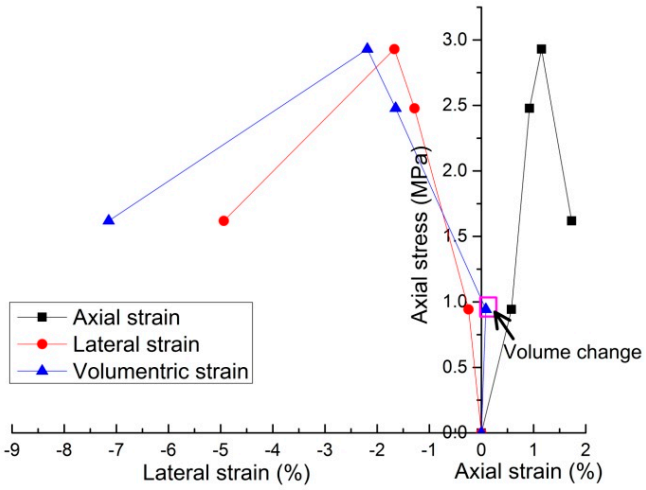

Figure 15. The axial, lateral, and volumetric stress strain curves at the five CT scanning points.

4. Conclusions

This paper presented the results of in-situ uniaxial compressive experiment on cemented waste rock backfill for the Lilou mining, using X-ray computed tomography (CT). A specially designed loading device had been used to match the high energy CT machine and it was demonstrated that the transparent X-ray loading device provided an excellent non-destructive tool for investigating the mesoscopic mechanical behaviors of the CWRB sample. The main findings from this study are summarized as follow:

(1) The experimental results indicated that the macroscopic mechanical behaviors of CWRB were affected by the meso-structural changes during sample deformation. The shape and distribution of the waste rocks influenced cracking distribution. Additionally, the crack propagation path was restricted by the waste rock size and shape.

(2) Meso-damage evolution of CWRB using the CT value clarified the damage propagation characteristics. The most severe damaged regions were located at the interfaces because of the stiff contrast between waste rock and tailing paste. Low-density regions in the CT images evolved into cracks and dilatancy became severe as deformations grew. The strain localization phenomenon, especially at the interfaces, was strongly influenced by the relative positions of the waste rock in CWRB.

(3) The X-ray CT data revealed that the damage evolution in CWRB was quite inhomogeneous. Stress dilatancy was an obvious phenomenon during the CWRB deformation because of the interactions between the waste rock and the cemented tailing paste. This may have influenced the stability of the pillar during mining activity, as its meso-mechanical behaviors were deeply studied.

(4) Although many macroscopic mechanical tests have been conducted for CWRB, the in-situ CT test was performed for only one CWRB sample, with a waste rock proportion of 30%. In the further study, CWRB samples with different rock proportions should be studied, in order to compare the meso-damage characteristics and the associated stress dilatancy behaviors.

Author Contributions: Y.W. and C.L. designed the theoretical framework; Y.W. conducted the experiments and wrote the manuscript; Z.H., X.Y., and X.W. corrected the figures.

Funding: This study was supported by National key technologies Research & Development program (2018YFC0808402, 2018YFC0604601, and 2017YFC0804103), the Fundamental Research Funds for the Central Universities (2302017FRF-TP-17-027A1), and National Natural Science Foundation of China (Grants Nos. 41502294).

Acknowledgments: The authors would like to thank the editors and the anonymous reviewers for their helpful and constructive comments.

Conflicts of Interest: The authors declare no conflict of interest.

References

1. Kesimal, A.; Yilmaz, E.; Ercikdi, B. Evaluation of paste backfill mixture consisting of sulphide-rich mill tailings and varying cement content. *Cem. Concr. Res.* **2004**, *34*, 1817–1822. [CrossRef]
2. Fall, M.; Benzaazoua, M.; Ouellet, S. Experimental characterization of the influence of tailings fineness and density on the quality of cemented paste backfill. *Miner. Eng.* **2005**, *18*, 41–44. [CrossRef]
3. Fall, M.; Benzaazoua, M. Modeling the effect of sulphate on strength development of paste backfill and binder mixture optimization. *Cem. Concr. Res.* **2005**, *35*, 301–314. [CrossRef]
4. Fall, M.; Pokharel, M. Coupled effects of sulphate and temperature on the strength development of cemented tailings backfills: Portland cement-paste backfill. *Cem. Concr. Compos.* **2013**, *32*, 819–828. [CrossRef]
5. Huang, Y.; Zhang, J.; Zhang, Q.; Nie, S. Backfilling technology of substituting waste and fly ash for coal underground in China coal mining area. *Environ. Eng. Manag. J.* **2011**, *10*, 110–119. [CrossRef]
6. Ke, X.; Hou, H.; Zhou, M.; Wang, Y.; Zhou, X. Effect of particle gradation on properties of fresh and hardened cemented paste backfill. *Constr. Build. Mater.* **2015**, *96*, 378–382. [CrossRef]
7. Belem, T.; Benzaazoua, M. Design and application of underground mine paste backfill technology. *Geotech. Geol. Eng.* **2008**, *26*, 147–174. [CrossRef]
8. Belem, T.; Benzaazoua, M. Predictive models for pre-feasibility cemented pastebackfill mix design. In Proceedings of the 3rd International Conference on Post-Mining, Nancy, France, 6–8 February 2008.
9. Cui, L.; Fall, M. An evolutive elasto-plastic model for cemented paste backfill. *Comput. Geotech.* **2016**, *71*, 19–29. [CrossRef]
10. Cayouette, J. Optimization of the paste backfill plant at Louvicourt mine. *CIM Bull.* **2003**, *96*, 51–57.
11. Fahey, M.; Helinski, M.; Fourie, A. Development of specimen curing proceduresthat account for the influence of effective stress during curing on the strengthof cemented mine backfill. *Geotech. Geol. Eng.* **2011**, *29*, 709–723. [CrossRef]
12. Chen, Q.S.; Zhang, Q.L.; Fourie, A.; Chen, X.; Qi, C.C. Experimental investigation on the strength characteristics of cement paste backfill in a similar stope model and its mechanism. *Constr. Build. Mater.* **2017**, *154*, 34–43. [CrossRef]
13. Cao, S.; Yilmaz, E.; Song, W. Evaluation of viscosity, strength and microstructural properties of cemented tailings backfill. *Minerals* **2018**, *8*, 352. [CrossRef]
14. Taheri, A.; Tatsuoka, F. Small-And large-Strain behaviour of a cement-treated soil during various loading histories and testing conditions. *Acta Geotech.* **2015**, *10*, 131–155. [CrossRef]
15. Wu, J.; Feng, M.; Chen, Z.; Mao, X.; Han, G.; Wang, Y. Particle size distribution effects on the strength characteristic of cemented paste backfill. *Minerals* **2018**, *8*, 322. [CrossRef]
16. Thomas, P.S.; Hirschausen, D.; White, R.E.; Guerbois, J.P.; Ray, A.S. Characterisation ofthe oxidation products of pyrite by thermogravimetric and evolved gas analysis. *J. Therm. Anal. Calorim.* **2003**, *72*, 769–776. [CrossRef]
17. Yilmaz, E.; Benzaazoua, M.; Belem, T.; Bussière, B. Effect of curing under pressureon compressive strength development of cemented paste backfill. *Miner. Eng.* **2009**, *22*, 772–785. [CrossRef]
18. Yilmaz, E.; Belem, T.; Bussière, B.; Benzaazoua, M. Relationships between microstructural properties and compressive strength of consolidated and unconsolidated cemented paste backfills. *Cem. Concr. Compos.* **2011**, *33*, 702–715. [CrossRef]
19. Jiang, H.; Fall, M. Yield stress and strength of saline cemented tailings in sub-zero environments: Portland cement paste backfill. *Int. J. Miner. Process.* **2017**, *160*, 68–75. [CrossRef]
20. Klein, K.; Simon, D. Effect of specimen composition on the strength development in cemented paste backfill. *Can. Geotech. J.* **2006**, *43*, 310–324. [CrossRef]
21. Fall, M.; Belem, T.; Samb, S.; Benzaazoua, M. Experimental characterization of the stress–strain behaviour of cemented paste backfill in compression. *J. Mater. Sci.* **2007**, *42*, 3914–3922. [CrossRef]
22. Zhang, J.; Deng, H.; Taheri, A.; Deng, J.; Ke, B. Effects of superplasticizer on the hydration, consistency, and strength development of cemented paste backfill. *Minerals* **2018**, *8*, 381. [CrossRef]
23. Zheng, J.; Zhu, Y.; Zhao, Z. Utilization of limestone powder and water-reducing admixture in cemented paste backfill of coarse copper mine tailings. *Constr. Build. Mater.* **2016**, *124*, 31–36. [CrossRef]
24. Xu, W.; Cao, P.; Tian, M. Strength development and microstructure evolution of cemented tailings backfill containing different binder types and contents. *Minerals* **2018**, *8*, 167. [CrossRef]

25. Li, W.; Fall, M. Sulphate effect on the early age strength and self-desiccation of cemented paste backfill. *Constr. Build. Mater.* **2016**, *106*, 296–304. [CrossRef]
26. Hane, I.; Belem, T.; Benzaazoua, M.; Maqsoud, A. Laboratory Characterization of Cemented Tailings Paste Containing Crushed Waste Rocks for Improved Compressive Strength Development. *Geotech. Geol. Eng.* **2017**, *35*, 645–662. [CrossRef]
27. Taheri, A.; Tatsuoka, F. Stress–strain relations of cement–mixed gravelly soil from multiple–step triaxial compression test results. *Soils Found.* **2012**, *52*, 748–766. [CrossRef]
28. Wu, J.Y.; Feng, M.M.; Yu, B.Y.; Chen, Z.Q.; Mao, X.B.; Han, G.S. Experimental study of strength and deformation characteristics of cemented waste rock backfills with continuous gradation. *Rock Soil Mech.* **2017**, *38*, 101–107.
29. He, G.C.; Liu, Y.; Ding, D.X.; Zhang, Z.J. Strength characteristic of cemented waste rock backfills and its application. *J. Min. Saf. Eng.* **2013**, *30*, 75–79.
30. He, G.C.; Liu, S.L.; Huang, B.X.; Zhang, Z.J.; Ding, D.X. Reasonable matching for cemented waste rock backfill and sand shale. *J. Min. Saf. Eng.* **2017**, *34*, 371–377.
31. Liu, C.; Han, B.; Sun, W.; Wu, J.X.; Yao, S.; Hu, H.Y. Experimental study of strength of back fillings of cemented rock debris and its application under low temperature condition. *Chin. J. Rock Mech. Eng.* **2015**, *34*, 139–147.
32. Du, X.J.; Feng, G.R.; Guo, Y.X.; Qi, T.Y.; Zhang, Y.J.; Guo, J. Failure analyses of unconfined CCWBM body in uniaxial compression based on central pressure variation. *Waste Manag. Res.* **2018**, *36*, 159–168. [CrossRef] [PubMed]
33. Anay, R.; Soltangharaei, V.; Assi, L.; DeVol, T.; Ziehl, P. Identification of damage mechanisms in cement paste based on acoustic emission. *Constr. Build. Mater.* **2018**, *164*, 286–296. [CrossRef]
34. Assi, L.; Anay, R.; Leaphart, D.; Soltangharaei, V.; Ziehl, P. Understanding Early Geopolymerization Process of Fly Ash–Based Geopolymer Paste Using Pattern Recognition. *J. Mater. Civ. Eng.* **2018**, *30*, 04018092. [CrossRef]
35. Hirono, T.; Takahashi, M.; Nakashima, S. In situ visualization of fluid flow image within deformed rock by X-ray CT. *Eng. Geol.* **2003**, *70*, 37–46. [CrossRef]
36. Cnudde, V.; Boone, M.N. High-resolution X-ray computed tomography in geosciences: A review of the current technology and applications. *Earth Sci. Rev.* **2013**, *123*, 1–17. [CrossRef]
37. Wang, Y.; Li, C.H.; Hao, J.; Zhou, R.Q. X-ray micro-tomography for investigation of meso-structural changes and crack evolution in Longmaxi formation shale during compressive deformation. *J. Pet. Sci. Eng.* **2018**, *164*, 278–288. [CrossRef]
38. Wang, Y.; Li, X.; Wu, Y.F.; Lin, C.; Zhang, B. Experimental study on meso-damage cracking characteristics of RSA by CT test. *Environ. Earth Sci.* **2015**, *73*, 5545–5558. [CrossRef]
39. *GB/T 208-94, Standard Test Method for Cement Density*; State Bureau of Technical Supervision: Beijing, China, 1994.
40. *GB/T 175-2007, Common Portland Cement*; SAI Global: Sydney, Australia, 2007.
41. *GB/T 50123-1999: Standard for Soil Test Method*; MWRPRC (Ministry of Water Resources of the People's Republic of China): Beijing, China, 1999.
42. Singh, U.K.; Digby, P.J. A continuum damage model for simulation of the progressive failure of brittle rocks. *Int. J. Solids Struct.* **1989**, *25*, 647–663. [CrossRef]
43. Lemaitre, J.; Chaboche, J.L. *Mechanics of Solid Materials*; Cambridge University Press: Cambridge, UK, 1990.
44. Zhou, X.P.; Zhang, Y.X.; Ha, Q.L. Real-time computerized tomography (CT) experiments on limestone damage evolution during unloading. *Theor. Appl. Fract. Mech.* **2008**, *50*, 49–56. [CrossRef]
45. Wang, Y.; Hou, Z.Q.; Hu, Y.Z. In situ X-ray micro-CT for investigation of damage evolution in black shale under uniaxial compression. *Environ. Earth Sci.* **2018**, *77*, 717. [CrossRef]

© 2018 by the authors. Licensee MDPI, Basel, Switzerland. This article is an open access article distributed under the terms and conditions of the Creative Commons Attribution (CC BY) license (http://creativecommons.org/licenses/by/4.0/).